RSC Advances

PAPER

View Article Online
View Journal | View Issue

Cite this: *RSC Adv.*, 2026, **16**, 15313

Non-enzymatic electrochemical glucose sensing using flexible rGO/AgNW@PANI composite films on nylon substrates

Ummul Kainatt, †[a] Nusrat Jahan Usha, †[a] Ayesha Binth Humayun, [a] Md Rakibul Hasan, [b] Arup Kumer Roy *[b] and Sumit Majumder *[a]

Received 7th January 2026
Accepted 12th March 2026

DOI: 10.1039/d6ra00166a

rsc.li/rsc-advances

A flexible non-enzymatic electrochemical glucose sensor was developed using rGO/AgNW@PANI composite films deposited on nylon substrates. The hybrid rGO/AgNW@PANI film serves as both a conductive and sensing layer, in which the rGO and Ag nanowires establish an efficient electron-transfer network, while polyaniline contributes electroactive sites that facilitate glucose oxidation in synergy with the composite architecture. The chemical composition and microstructural features of the composite films were confirmed by FT-IR, FE-SEM, EDS, and XPS analyses. The resulting sensor exhibits a linear electrochemical response to glucose over a concentration range of 0.01–0.1 mM (R^2 = 0.99), with a sensitivity of 2.9 mA mM^{-1} cm^{-2}, a detection limit of 0.01 mM, and a rapid response time in phosphate-buffered saline (PBS) solution (pH ≈ 6.5). Additionally, the flexible sensor demonstrates excellent mechanical robustness and long-term stability during repeated glucose sensing. These results highlight the potential of flexible rGO/AgNW@PANI composite films on nylon substrates as a promising platform for non-enzymatic electrochemical glucose sensing, with potential relevance to future flexible and wearable sensing applications.

Introduction

Diabetes is a chronic metabolic disorder characterized by elevated blood glucose levels above the normal range of 80–120 mg dL^{-1} (4.4–6.6 mM), arising from insulin insufficiency and impaired glucose regulation.[1] Globally, an estimated 150 million individuals are affected by diabetes and related complications, which contribute significantly to morbidity, including kidney failure, blindness, and neuropathy, and can increase the risk of mortality.[2,3] The World Health Organization (WHO) projects that by 2035, the number of people with diabetes will reach 592 million,[4] potentially making it the seventh leading cause of death worldwide by 2030.[5] Currently, there is no complete pharmacological cure for diabetes, and disease management relies on frequent blood glucose monitoring.[6] Accurate assessment and regulation of glucose levels are therefore critical for diagnosis and therapeutic intervention. In this context, flexible glucose sensors can potentially offer distinct advantages for real-world and clinical applications, enabling continuous, non-invasive, or minimally invasive monitoring, while enhancing patient comfort and supporting improved disease management.

Glucose sensors fall into two major categories: enzymatic and non-enzymatic. Enzymatic glucose sensors have dominated the market for decades due to their high specificity and sensitivity.[7] Nevertheless, enzymatic sensors are generally expensive due to the high cost and instability of purified enzymes.[8] Furthermore, their performance can be adversely affected by environmental factors such as temperature, pH, ionic strength, and the presence of inhibitors.[9,10] Additionally, degradation of enzymes over time can reduce sensor accuracy and sensitivity.[11] In contrast, non-enzymatic glucose sensors provide a promising cost-effective alternative for glucose monitoring in biofluids such as sweat, urine, tears, interstitial fluids and saliva. By eliminating reliance on biological components, non-enzymatic sensors offer greater stability and robustness,[12,13] while enabling minimally invasive or non-invasive glucose monitoring with reduced risk of discomfort or infection. Additionally, these sensors can operate over broader temperature and pH ranges,[10] making them suitable for diverse clinical and real-world conditions.

In non-enzymatic electrochemical glucose sensors, the electrode material plays a key role in determining the sensitivity and specificity of glucose detection. Typically, these sensors employ a three-electrode configuration comprising a working, reference, and counter electrode.[14] The working electrode functions as the active sensing element, where glucose undergoes electrochemical oxidation or reduction, generating electrons. The reference electrode (commonly Ag/AgCl) provides a stable potential, while the counter electrode (*e.g.*, Pt or glassy carbon) completes the electrical circuit by allowing current to

[a]*Department of Biomedical Engineering, Chittagong University of Engineering and Technology, Chattogram-4349, Bangladesh. E-mail: s.majumder@cuet.ac.bd*

[b]*Department of Chemistry, Chittagong University of Engineering and Technology, Chattogram-4349, Bangladesh. E-mail: arupkumer@cuet.ac.bd*

† These authors contributed equally to this work.

flow through the electrolyte. The electrons produced at the working electrode generate a measurable current that is directly proportional to the glucose concentration.

Various conducting polymers, including polyaniline (PANI),[15–17] polypyrrole (PPy),[18,19] polythiophene (PTh),[20,21] and poly(3,4-ethylenedioxythiophene) (PEDOT),[22,23] have been investigated as functional components in composite working electrodes for non-enzymatic glucose sensors. Among these, polyaniline (PANI) has received particular attention due to its unique redox behavior, high electrical conductivity, and environmental stability.[24,25] PANI can reversibly switch between leucoemeraldine, emeraldine, and pernigraniline oxidation states, rendering it highly responsive to the redox reactions involved in glucose detection.[26] However, pure PANI exhibits poor long-term stability under electrochemical conditions, including potential degradation and reduced activity in acidic or alkaline environments.[27,28] Incorporating carbon nanomaterials (*e.g.*, graphene, carbon nanotubes, carbon quantum dots)[29] and metal nanoparticles (Ag, Au, Pt, Cu)[30] into PANI enhances conductivity, increases effective surface area, and improves catalytic performance. Moreover, PANI functions as a conductive component, promoting efficient electron transport while enabling robust and reproducible electrode fabrication.[31]

In this manuscript, we report the fabrication of a flexible non-enzymatic glucose sensor based on an rGO/AgNW@PANI composite film on a nylon filter membrane substrate. The rGO/AgNWs composite was first deposited onto a nylon substrate *via* vacuum filtration. The resulting surface was then coated with a PANI solution using spray deposition. In the resulting working electrode, rGO sheets and AgNWs form an interconnected conductive network that facilitates efficient electron transport and increases the electrochemically accessible surface area, while PANI serves both as a conductive matrix and as the electroactive material responsible for glucose oxidation. The sequential vacuum filtration and spray-coating approach enables effective PANI deposition while preserving the porous structure and inherent mechanical flexibility of the nylon membrane, thereby providing a mechanically robust platform suitable for flexible and wearable electrochemical sensing applications.

Experimental details

Materials and reagents

Graphite flakes (No. 1, +50 mesh, Dixon Ticonderoga), potassium permanganate ($KMnO_4$, Merck), sulfuric acid (H_2SO_4, 98%, Merck), sodium hydroxide (NaOH, Merck), silver nitrate ($AgNO_3$, Merck), sodium chloride (NaCl, Merck), D-(+)-glucose (ACS reagent grade, Macklin), ethylene glycol (anhydrous, 99.8%), *N*-methyl-2-pyrrolidone (NMP, Macklin), polyaniline (emeraldine salt, M_w > 15 000, Sigma), polyethylene glycol (PEG6000, Merck), potassium bromide (KBr, Merck), polyvinylpyrrolidone (PVP, $M_n \approx 40\,000$, Merck), absolute ethanol (Merck), and isopropyl alcohol (IPA, Merck) were used as received without further purification. Deionized water (18.2 MΩ cm) was obtained from a Millipore-Q system. Nylon 6,6 membrane collected from Pall corporation, India.

Apparatus

Fourier transform infrared (FT-IR) spectra were recorded using a PerkinElmer Spectrum FT-IR spectrometer over the range of 400–4000 cm^{-1}. Surface morphology and elemental composition were examined by field-emission scanning electron microscopy (FE-SEM) coupled with energy-dispersive X-ray spectroscopy using a JEOL JSM-6010LA instrument. X-ray photoelectron spectroscopy (XPS) measurements were performed on a Thermo Scientific K-Alpha system equipped with a hemispherical electron analyzer and a microfocused monochromatic Al Kα radiation source. Voltammetric measurements were carried out using a portable Metrohm μStat 300 bipotentiostat in a standard three-electrode configuration. All characterizations were conducted on nylon-supported composite film electrodes.

Synthesis of reduced graphene oxide (rGO)

Expanded graphite flakes were prepared from mesh graphite flakes (+50 mesh) *via* controlled chemical oxidation followed by thermal expansion. First, 3 g of $KMnO_4$ was slowly added to 60 mL of concentrated H_2SO_4 under ice-bath cooling to control the highly exothermic reaction. Subsequently, 1.5 g of graphite flakes were introduced and stirred at 300 rpm for 10 min. The stirring was then stopped, and the mixture was left at room temperature overnight. The reaction mixture was diluted with deionized water, followed by decantation to remove the supernatant. The remaining solid was collected using a PTFE membrane filter (0.45 μm) and washed repeatedly with deionized water until a neutral pH was achieved, followed by drying at 80 °C. The dried material was subsequently thermally expanded in a muffle furnace at 600–700 °C to obtain expanded graphite flakes (EGF).

Graphene oxide (GO) was synthesized from EGF following a modified Tour's method.[32] In this procedure, 1 g of EGF was dispersed in a mixture of H_2SO_4 and H_3PO_4 (9 : 1 v/v, 9 mL total) and sonicated in an ice bath for 30–60 min. Separately, an oxidizing solution consisting of H_2SO_4 and H_3PO_4 (9 : 1 v/v, 40 mL total) was prepared and cooled in an ice bath, after which 7 g of $KMnO_4$ was gradually added under continuous cooling to prevent rapid temperature rise and uncontrolled reactions.

The prepared oxidizing solution was then transferred to a burette and added dropwise to the EGF dispersion under continuous stirring. The resulting mixture was stirred at 300 rpm and maintained at 35 °C for 12 h. The reaction was quenched by the gradual addition of 200 mL of ice-cold deionized water, with subsequent addition of 3 mL of H_2O_2, resulting in a colour change from dark brown to yellowish brown. The diluted graphene oxide (GO) was separated from the acidic medium by PTFE membrane filtration and washed repeatedly with 5% HCl solution (200 mL) and deionized water until the pH reached approximately 6. The collected GO was subsequently redispersed in deionized water using bath sonication, and any remaining unexfoliated residues were removed by centrifugation. The double oxidation process enhances graphite exfoliation and increases the density of oxygen-containing functional groups,[33] yielding highly oxidized GO

with improved dispersibility and surface functionality that facilitates its integration with Ag nanowires (AgNWs) and the PANI matrix in the composite electrode.

Reduced graphene oxide (rGO) was prepared by chemically reducing the GO dispersion with ascorbic acid. In this process, 0.5 g of ascorbic acid was added to the GO solution, and the mixture was stirred at 80 °C until black flocculates formed, indicating successful reduction. The rGO was collected by centrifugation at 8000 rpm for 10 min and dried at room temperature for film fabrication, or at 60 °C to obtain rGO powder.

Synthesis of silver nanowires (AgNWs)

Silver nanowires (AgNWs) were synthesized *via* a hydrothermal method reported previously.[34] In a typical procedure, separate solutions of $AgNO_3$ (0.02 M, 30 mL), D-(+)-glucose (0.12 g, 10 mL), KBr (0.02 g, 20 mL), and NaCl (0.04 g, 30 mL) were prepared in deionized water at room temperature. Meanwhile, polyvinylpyrrolidone (PVP, $M_n \approx 40\,000$, 2 g in 10 mL water) was dissolved at 65 °C. The synthesis was initiated by adding the D-(+)-glucose solution to the $AgNO_3$ solution under continuous stirring. D-(+)-Glucose was used as a mild reducing agent to gradually reduce Ag^+ ions to metallic Ag^0, enabling controlled nucleation and anisotropic growth of Ag nanowires during hydrothermal synthesis.[34,35]

After 10 min, the PVP solution was slowly introduced until the mixture became homogeneous, where PVP acted as a capping agent, thus controlling the growth of the nanowires.[36] Subsequently, the NaCl and KBr solutions were added dropwise under stirring until fully dissolved. The resulting solution was transferred to a 100 mL polyphenylene-lined (PPL) stainless steel autoclave and heated in an oven at 160 °C for 24 h. After natural cooling to room temperature, the gray precipitate was collected by centrifugation (2500 rpm, 30 min), washed with isopropanol (IPA), and redispersed in IPA for further use.

Preparation of polyaniline (PANI)

A commercial polyaniline (PANI) solution was prepared by dissolving 0.15 g of PANI in 5 mL of *N*-methyl-2-pyrrolidone (NMP) under continuous stirring. The mixture was then sonicated for 30 min to disrupt any aggregates and obtain a clear, homogeneous solution. The resulting solution was kept at room temperature and used in subsequent sensor fabrication steps.

Fabrication of rGO/AgNW@PANI composite film

For the fabrication of the rGO/AgNWs@PANI composite film, a flexible nylon substrate (0.45 μm pore size) was used as the substrate. The process began by dispersing 1 g of rGO in 10 mL of *N*-methyl-2-pyrrolidone (NMP) *via* sonication. Subsequently, 0.03 g of AgNWs were added to the rGO dispersion under continuous stirring to obtain a uniform mixture. In a separate step, 0.3 g polyethylene glycol (PEG) was dissolved in 10 mL of deionized water and incorporated into the rGO/AgNWs suspension, where PEG served as a binder. The resulting homogeneous mixture was deposited onto the nylon substrate *via* vacuum filtration. The physical and chemical interactions between rGO and the nylon substrate imparted long-term stability, while the nylon substrate enhanced the flexibility, durability, and mechanical toughness of the composite (Fig. 1).[37,38]

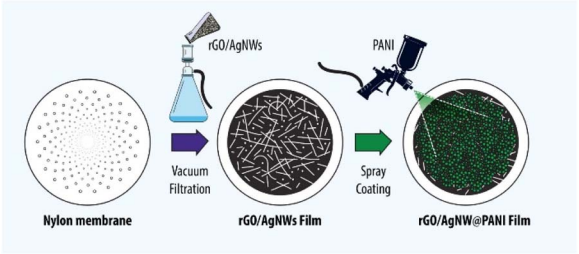

Fig. 1 Fabrication process of rGO/AgNW@PANI composite film.

Bare PANI deposited on nylon substrate was observed to become loosely bound and prone to dispersion into the electrolyte within a few days. Therefore, freshly prepared PANI membranes dried for one hour were used for glucose sensing. To complete the composite, 0.5 mL of PANI solution was uniformly sprayed onto the rGO/AgNWs layer using a spray-coating technique. The composite film was thoroughly washed with ethanol to remove residual NMP and other impurities and then dried at 60–70 °C to enhance mechanical stability, interlayer adhesion, and electrical performance.

Preparation of the modified electrode film

Electrochemical glucose detection was carried out using a standard three-electrode system, in which a nylon-supported rGO/AgNW@PANI composite film served as the working electrode, with Ag/AgCl and a Teflon-coated Pt sheet as the reference and counter electrodes, respectively. The working electrode had dimensions of 1.2 × 1.2 cm, corresponding to an area of 1.44 cm^2. The flexible composite film was secured to the PTFE-coated electrode holder with a clamp and immersed in the electrolyte solution. The electrolyte consisted of 0.1 M phosphate-buffered saline (PBS, pH 6.5), with the pH adjusted using HCl or NaOH as required (Fig. S1).

Results and discussion

The electrochemical glucose-sensing mechanism using rGO/AgNW@PANI is illustrated in Fig. 2. Upon reaching the composite film surface, glucose molecules undergo electrochemical oxidation under the applied potential.

At the anodic electrode, glucose is oxidized, losing electrons to form gluconolactone and generating an electrical current, which can be measured *via* an external circuit. The overall oxidation reaction of glucose at the electrode is represented as:

$$\text{Glucose } (C_6H_{12}O_6) \rightarrow \text{Gluconolactone } (C_6H_{11}O_7^-) + 2H^+ + 2e^-$$

Mechanism of glucose sensing on the rGO/AgNW@PANI film

In the electrochemical analysis for glucose detection, the flexible rGO/AgNWs composite film served as a highly conductive support with catalytically active sites, while the spray-coated PANI

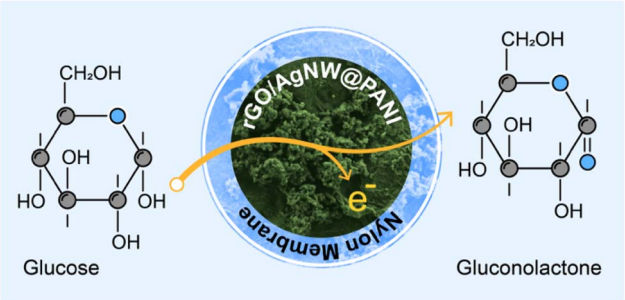

Fig. 2 Sensing mechanism of non-enzymatic glucose sensor based on rGO/AgNW@PANI nanocomposite film.

functioned as both a conductive component and the electroactive sensing material.[39] PANI exhibits excellent electrochemical properties, including reversible redox behavior, electrochemical tunability, processability, and long-term stability.[40] Glucose oxidation occurs under an applied potential through interactions between glucose hydroxyl (–OH) groups and PANI C–N functionalities, mediated by van der Waals forces, hydrogen bonding, and electrostatic interactions, thereby producing a measurable electrical current.[41] The combination of rGO/AgNWs and PANI enhances sensor performance by improving conductivity, sensitivity, and electrochemical stability through their complementary functional roles.[42]

Characterization rGO/AgNW@PANI film

Although PANI-based electrodes are capable of glucose detection,[41] they do not efficiently catalyze glucose oxidation. The incorporation of rGO and metal nanostructures, such as AgNWs, improves electrical conductivity and increases the effective surface area. The introduction of AgNWs within the rGO network enhances ion diffusion pathways and catalytic activity, leading to improved sensing characteristics.[43] Consequently, the PANI-coated rGO/AgNWs composite film exhibits superior non-enzymatic glucose detection performance. In this architecture, PANI serves as the conductive and electroactive sensing component, while the rGO/AgNWs network enhances charge transport and facilitates efficient electron transfer during electrochemical sensing.[44] The components of the rGO/AgNW@PANI composite interact primarily through non-covalent interactions, including π–π stacking between PANI and rGO, hydrogen bonding involving oxygen-containing functional groups on rGO, and weak electrostatic interactions associated with the PVP-coated AgNWs surface.[45–47] The resulting composite film is deposited onto a nylon substrate *via* vacuum filtration, providing a flexible and mechanically robust sensing platform.

Electrochemical study of rGO/AgNW@PANI for glucose sensing

To evaluate the non-enzymatic glucose sensing performance of the nylon-supported rGO/AgNW@PANI electrode, cyclic voltammetry (CV) measurements (scan rate 20 mV s^{-1}) were conducted in 0.1 M PBS (pH 6.5) containing glucose concentrations ranging from 0.01 to 0.1 mM, a range selected to closely match the physiological glucose levels typically found in human sweat (0.06–0.2 mM) for wearable, non-invasive monitoring applications (Fig. 3).[48]

For comparison, the CV responses of the bare nylon-supported Pt electrode, PANI-coated nylon electrode, rGO/AgNWs and rGO/AgNW@PANI composite film electrode were recorded in the presence of glucose (Fig. 3a). The bare Pt electrode exhibited negligible current densities and no discernible redox features within the potential window of −1.0 to +1.0 V. The potential window of −1.0 to 1.0 V was selected to capture the characteristic redox transitions of PANI and the glucose oxidation response while maintaining stable electrochemical conditions in the PBS electrolyte.[49,50]

The PANI electrode showed a weak oxidation peak at approximately +0.2 V. In contrast, the rGO/AgNW@PANI electrode displayed a pronounced quasi-reversible redox response, with an enhanced oxidation peak appearing in the 0.2–0.4 V range, confirming its superior electrochemical activity toward glucose oxidation. The slight positive shift in the oxidation peak potential relative to bare PANI is attributed to improved charge transport and electronic coupling arising from the incorporation of rGO and AgNWs.[51,52]

Notably, the rGO/AgNWs electrode alone did not exhibit a distinct glucose oxidation peak within the investigated potential range (Fig. 3a), indicating that rGO/AgNWs primarily

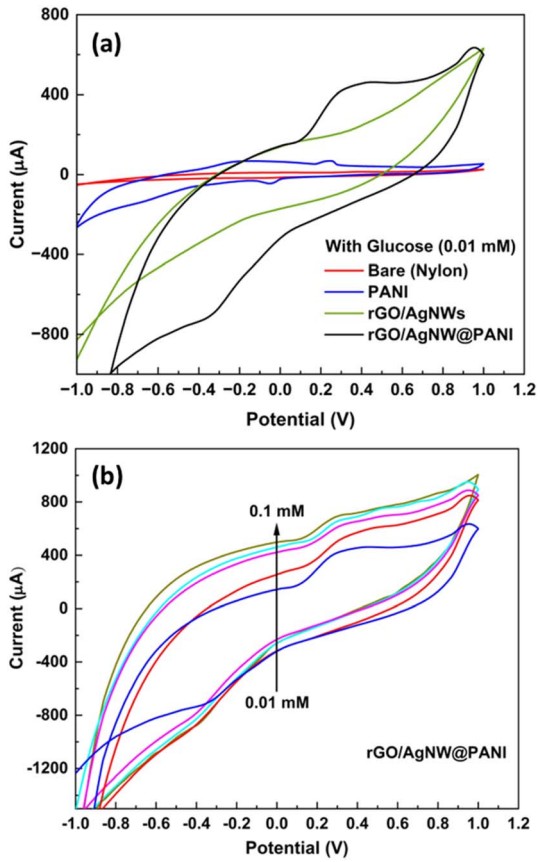

Fig. 3 Glucose sensing performance: (a) cyclic voltammetry (CV) curves of bare electrode, PANI, rGO/AgNWs and rGO/AgNW@PANI; (b) calibration curve for glucose detection at different concentrations using the rGO/AgNW@PANI film.

act as a conductive framework rather than an active sensing component. The incorporation of PANI onto the rGO/AgNWs framework increases the effective electroactive surface area and facilitates electron-transfer kinetics during the electrochemical reaction.[53] In the absence of glucose, no anodic peak was observed within this potential region (Fig. S2), confirming the glucose-specific response of the electrode. As shown in Fig. 3b, the anodic peak current increases systematically with increasing glucose concentration (0.01–0.1 mM), consistent with the electrochemical oxidation of glucose to gluconolactone. The PANI-modified electrode exhibits its highest response current and sensitivity in PBS at pH ≈ 6.5, while at pH ≈ 7.4, PANI undergoes partial deprotonation from its electroactive emeraldine salt form to the less conductive emeraldine base form (Fig. S3), resulting in a pronounced decrease in conductivity and electron-transfer efficiency.[54,55] Accordingly, PBS at pH 6.5 was selected as the optimal supporting electrolyte for glucose sensing.

The long-term stability of the rGO/AgNW@PANI sensor was assessed by comparing CVs recorded before and after three months of storage (Fig. S4) under ambient conditions in 0.1 M PBS (pH 6.5). The electrode maintained a consistent electrochemical response, indicating that its activity is largely preserved over time. Minor performance changes are likely due to surface oxidation of AgNWs, while the rGO network and PANI matrix help maintain conductivity and structural integrity, supporting the sensor's suitability for prolonged non-enzymatic glucose monitoring.[56]

Morphology study

Field emission scanning electron microscopy (FE-SEM) was employed to examine the surface morphology of the fabricated films. All samples for FE-SEM characterization were prepared by depositing the respective onto 0.45 μm nylon substrate substrates. As shown in Fig. S5a, the pristine nylon substrate exhibits a highly porous, non-woven structure composed of interconnected microfibers. Following PANI deposition, this porous network is coated with fibrous and granular PANI nanostructures, as shown in Fig. S5b. The inset highlights the characteristic aggregated granular morphology of PANI.

For FE-SEM analysis of the rGO/AgNWs composite film, the rGO/AgNWs dispersion in NMP was deposited onto the nylon substrate by vacuum filtration, followed by ethanol washing and drying at 60–70 °C. As shown in Fig. 4a, the composite film exhibits an interconnected network in which AgNWs are embedded within and partially wrapped by wrinkled, sheet-like rGO layers. The wrinkling of rGO is attributed to structural defects such as pores and vacancies introduced during the reduction process, as well as local strain in the C–C bonds,[52,57] and may be further influenced by relaxation of the thermally treated nylon substrate.[58,59] This architecture forms a continuous conductive network, where rGO provides a flexible, high-surface-area scaffold and AgNWs act as highly conductive pathways that facilitate efficient electron transport. Most AgNWs are embedded within or anchored to the rGO sheets, ensuring intimate interfacial contact.

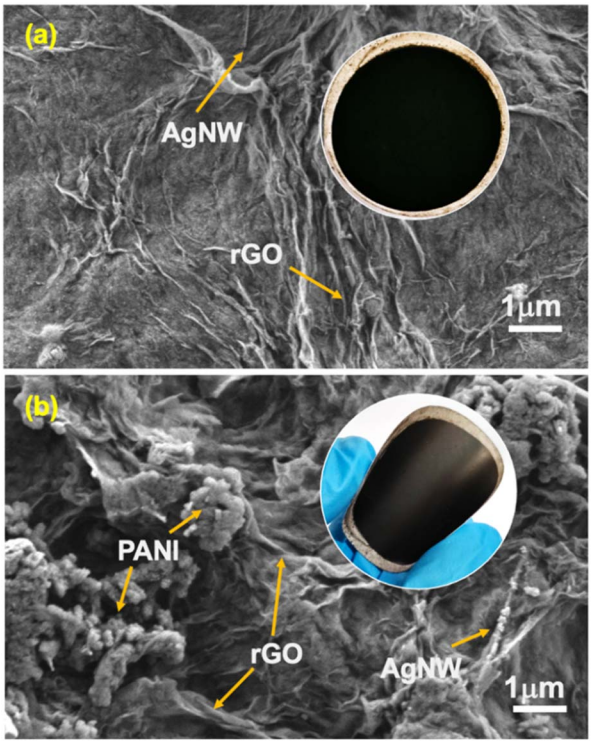

Fig. 4 FE-SEM images of (a) rGO/AgNWs (b) rGO/AgNW@PANI film.

After spray coating PANI onto the rGO/AgNWs membrane, granular and aggregated PANI nanostructures are observed to be randomly distributed across the surface and within the porous network, as shown in Fig. 4b. The PANI morphology closely resembles that observed for PANI deposited directly on nylon (Fig. S5b), confirming the successful incorporation of PANI onto the rGO/AgNWs framework while preserving its characteristic nanostructured morphology. Despite localized aggregation of PANI, the porous rGO/AgNWs framework remains exposed,[60] thereby preserving efficient charge transport pathways and electrochemically accessible surface sites.

Structure study

The Fourier transform infrared (FT-IR) spectra of PANI, rGO/AgNWs, and rGO/AgNW@PANI composite films deposited on nylon substrates are shown in Fig. 5a. For pristine PANI, a broad absorption band at approximately 3330–3400 cm^{-1} is attributed to N–H stretching vibrations of amine groups. The characteristic bands at ~1560–1575 cm^{-1} and ~1480–1495 cm^{-1} correspond to the C=C stretching vibrations of quinoid and benzenoid rings, respectively, confirming the emeraldine oxidation state of PANI. The peak observed at ~1290–1300 cm^{-1} is assigned to C–N stretching of aromatic amine units,[61] while the band near ~1130–1150 cm^{-1} is associated with in-plane C–N or C=N vibrations,[62] which are often considered indicative of the conducting protonated form of PANI. Additional bands at ~820–860 cm^{-1} arise from C–H out-of-plane bending vibrations of para-substituted benzene rings, further confirming the PANI backbone structure.[62]

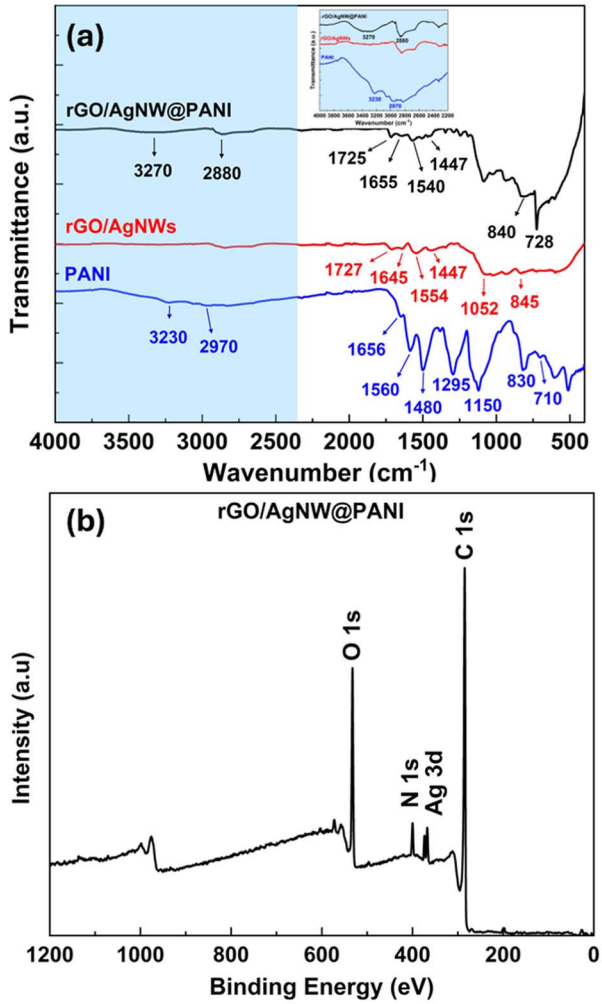

Fig. 5 (a) Comparative FT-IR spectra of all samples and (b) XPS survey spectra of rGO/AgNW@PANI.

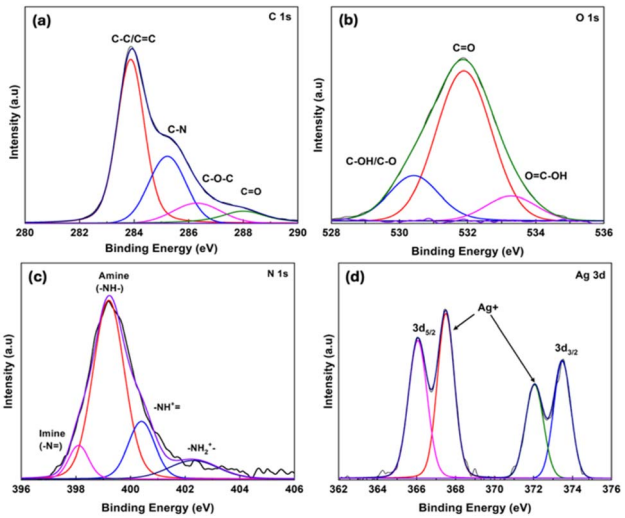

Fig. 6 Deconvoluted high-resolution XPS spectra of rGO/AgNW@PANI: (a) C 1s, (b) O 1s, (c) N 1s and (d) Ag 3d.

The FT-IR spectrum of the rGO/AgNWs film exhibits a weak band around ~1640–1650 cm^{-1}, attributed to the C=C stretching of sp^2-hybridized carbon domains in rGO.[61] A significantly attenuated carbonyl (C=O) stretching band near ~1720–1730 cm^{-1} is observed, indicating the effective reduction of graphene oxide.[63] The absence of a broad O–H stretching band in the 3200–3600 cm^{-1} region further supports the successful removal of oxygen-containing functional groups during reduction. Minor bands in the 1400–1500 cm^{-1} range correspond to residual aromatic C=C vibrations within the rGO framework. A new peak near ~840–850 cm^{-1} is attributed to out-of-plane bending vibrations associated with pyrrolidone rings, confirming the presence of PVP capping on the AgNWs surface.[64]

For the rGO/AgNW@PANI composite film, the characteristic PANI absorption bands are retained but exhibit slight shifts in position, notably the N–H stretching band at ~3260–3300 cm^{-1} and the quinoid and benzenoid C=C stretching bands near ~1540 cm^{-1} and ~1450 cm^{-1}, respectively.[61,65] These shifts indicate strong interfacial interactions between PANI and the rGO/AgNWs network, arising from π–π stacking, hydrogen bonding, and electronic coupling.[46,47,61,65] The preservation of key PANI vibrational features, together with their systematic shifts, confirms the successful incorporation of PANI onto the rGO/AgNWs framework and indicates interfacial interactions that contribute to enhanced conjugation and charge transport within the composite film.

Wide-scan X-ray photoelectron spectroscopy (XPS) survey spectra of the rGO/AgNW@PANI composite film were acquired to investigate its surface elemental composition. As shown in Fig. 5b, four dominant peaks are observed at binding energies of approximately 284, 368–374, 400, and 531 eV, corresponding to C 1s, Ag 3d, N 1s, and O 1s, respectively. These results confirm the successful incorporation of rGO, AgNWs, and PANI within the composite film, demonstrating strong interfacial interactions that are essential for enhanced charge transport and electrochemical performance.

The deconvoluted C 1s spectrum (Fig. 6a) reveals four components located at approximately 283.9, 285.4, 287.2, and 288.1 eV, corresponding to C–C/C=C (sp^2 carbon), C–N, C–O–C, and C=O functional groups, respectively.[66] These features confirm the coexistence of graphitic carbon from rGO and nitrogen-containing moieties from the PANI backbone. The O 1s spectrum (Fig. 6b) displays contributions at approximately 530.4, 531.8, and 533.3 eV, which are attributed to C=O, C–O/C–OH, and C–O–C species, respectively, arising primarily from residual oxygen-containing functional groups in rGO.

The high-resolution N 1s spectrum (Fig. 6c) was deconvoluted into four distinct peaks located at approximately 398.1, 399.2, 400.4, and 402.3 eV, corresponding to quinoid imine (–N=), benzenoid amine (–NH–), protonated imine ($–NH^+=$), and protonated amine ($–NH_2^+–$) species, respectively. These nitrogen environments are characteristic of polyaniline in its emeraldine salt form and confirm the successful incorporation of electroactive PANI within the composite structure.[46,67]

The high-resolution Ag 3d spectrum, shown in Fig. 6d, exhibits two prominent peaks centered at approximately

366.5 eV and 372.1 eV, which are assigned to the Ag $3d_{5/2}$ and Ag $3d_{3/2}$ spin–orbit components of metallic silver (Ag^0), respectively.[68] A weak shoulder at slightly higher binding energies indicates the presence of Ag^+ species, which can be attributed to partial surface oxidation and coordination interactions between AgNWs and the polyvinylpyrrolidone (PVP) capping agent.[69,70]

The XPS results are fully consistent with the FT-IR analysis, jointly confirming the successful formation and interfacial coupling of the rGO/AgNW@PANI composite, as evidenced by the correspondence between the quinoid and benzenoid PANI bands in the FT-IR spectra (Fig. 4a) and the quinoid imine (–N=) and benzenoid amine (–NH–) components in the N 1s XPS spectrum (Fig. 6c), the agreement between C–N and C=C vibrations observed in FT-IR (Fig. 4a) and the C 1s deconvoluted peaks in XPS (Fig. 6a), and the matching oxygen-containing functional groups (C–O, C=O, C–O–C) detected by FT-IR (Fig. 4a) and the O 1s spectrum (Fig. 6b), collectively verifying the composite's chemical integrity and effective interfacial interactions.

Energy-dispersive X-ray spectroscopy (EDS) analysis confirms the successful incorporation of PANI into the rGO/AgNWs composite film. As shown in Fig. S6, the mass fractions of carbon and nitrogen increase following PANI deposition, with the carbon content rising from 56.54% to 58.12% and the nitrogen content increasing from 2.57% to 3.51% compared with the pristine rGO/AgNWs film. These increases are attributed to the carbon-rich conjugated backbone of PANI and its nitrogen-containing amine and imine functionalities. In contrast, the mass percentages of silver and oxygen remain nearly unchanged, indicating that the PANI coating does not disrupt the underlying rGO/AgNWs framework.

Amperometric characteristics of rGO/AgNW@PANI composite film

Fig. 7 shows a linear increase in the electrode response with rising glucose concentration, demonstrating that the rGO/AgNW@PANI electrode exhibits an effective electrochemical response toward glucose (0.01–0.1 mM). The calibration curve

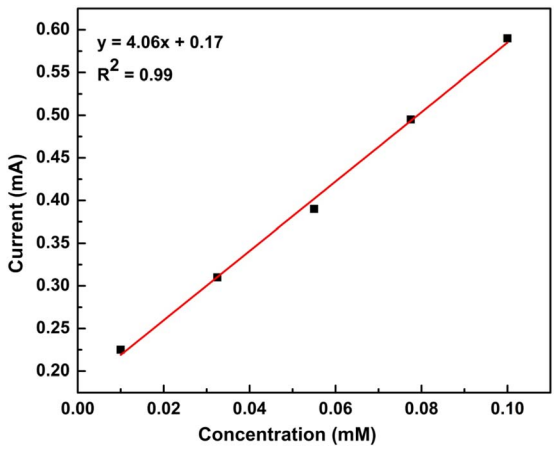

Fig. 7 Calibration curve between the peak current and the concentration of glucose with rGO/AgNW@PANI composite film.

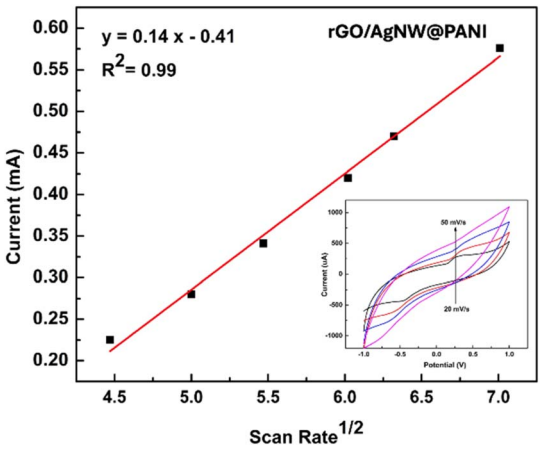

Fig. 8 Linear relationship between the peak current and the square root of the scan rate of the rGO/AgNW@PANI. The inset shows the voltammograms at different scan rates.

follows the linear equation $y = 4.06X + 0.17$ with an R^2 value of 0.99, indicating excellent linearity. Based on the slope normalized to the electrode area, the sensor sensitivity was determined as 2.9 mA mM^{-1} cm^{-2}, and the limit of detection (LOD) was 0.01 mM, calculated based on the standard deviation of the regression line and the slope.

In typical electrochemical systems, parameters such as the peak current (i_p), number of electrons transferred (n), electrode area (A), analyte concentration (C), diffusivity (D), and potential scan rate (v) are constant, making i_p proportional to $v^{0.5}$. As shown in Fig. 8, the linear relationship between the peak current (i_p) and the square root of the scan rate confirms a diffusion-controlled electrochemical process, validating the rGO/AgNW@PANI electrode as an appropriate platform for sensitive glucose detection.

Conclusions

In conclusion, flexible rGO/AgNW@PANI composite films were successfully fabricated on nylon substrates and demonstrated as an effective platform for non-enzymatic electrochemical glucose sensing. Within the sensor, the rGO/AgNWs network provides an efficient electron-transfer pathway, while PANI functions both as a conductive component and as the electroactive material that facilitates glucose oxidation, collectively enabling a rapid and reproducible electrochemical response. The resulting sensor exhibits a linear response to glucose concentrations in the physiologically relevant sweat range of 0.01–0.1 mM, with a sensitivity of 2.9 mA mM^{-1} cm^{-2}, a detection limit of 0.01 mM, and a rapid, reproducible electrochemical response in PBS (pH ≈ 6.5), making it well-suited for non-invasive wearable glucose monitoring applications. In addition, the sensor demonstrates good mechanical flexibility and long-term signal stability during repeated glucose measurements. These results indicate that nylon-supported rGO/AgNW@PANI composite films represent a promising and robust platform for flexible non-enzymatic

electrochemical glucose sensing, with potential relevance to future wearable and continuous monitoring applications.

Author contributions

The research is conceptualized and methodology was designed by Sumit Majumder and Arup Kumer Roy. Experiments were carried out by Ummul Kainatt, Nusrat Jahan Usha, and Md Rakibul Hasan. Formal analysis was conducted by Ummul Kainatt, Nusrat Jahan Usha, Ayesha Binth Humayun and Arup Kumer Roy. Writing – review and editing was undertaken by Sumit Majumder, Arup Kumer Roy, and Ayesha Binth Humayun. Supervision and project administration were carried out by Arup Kumer Roy and Sumit Majumder.

Conflicts of interest

There are no conflicts to declare.

Data availability

The data supporting this article have been included as part of the supplementary information (SI). Supplementary information: additional experimental data supporting the findings of this study, including the electrochemical sensing setup, comparative cyclic voltammetry responses of the rGO/AgNW@PANI electrode with and without glucose, pH-dependent electrochemical behavior, long-term stability measurements, and FE-SEM and EDS characterization of the electrode materials. See DOI: https://doi.org/10.1039/d6ra00166a.

Acknowledgements

This work was supported by the Directorate of Research and Extension (DRE) at Chittagong University of Engineering and Technology under project code CUET/DRE/2025-2026/BME/001.

References

1 J. Wang, *Electrochem. Sensors, Biosens. their Biomed. Appl.*, 2008, vol. 57, pp. 1–69.
2 E. Reitz, W. Jia, M. Gentile, Y. Wang and Y. Lei, *Electroanalysis*, 2008, **20**, 2482–2486, DOI: 10.1002/elan.200804327.
3 Z. Zhu, L. Garcia-Gancedo, A. J. Flewitt, H. Xie, F. Moussy and W. I. Milne, *Sensors*, 2012, **12**, 5996–6022, DOI: 10.3390/s120505996.
4 P. Khetrapal Singh, Prevent, control diabetes, https://www.who.int/southeastasia/news/detail/13-11-2015-prevent-control-diabetes, accessed 22 December 2025.
5 What are the consequences of diabetes?, https://www.emro.who.int/right-teasers/diabetes-info/what-are-the-consequences-of-diabetes.html, accessed 22 December 2025.
6 Y. Wang, F. Chen, J. Ye, H. Liu, T. Zhang and Z. Li, *Cellulose*, 2023, **30**, 5131–5143, DOI: 10.1007/s10570-023-05149-0.
7 K. V. Jarnda, D. Wang, Q. U. Ain, R. Anaman, V. E. Johnson, G. P. Roberts, P. S. Johnson, B. W. Jallawide, T. Kai and P. Ding, *Sensors Actuators A Phys.*, 2023, **363**, 114778, DOI: 10.1016/j.sna.2023.114778.
8 W. C. Lee, K. B. Kim, N. G. Gurudatt, K. K. Hussain, C. S. Choi, D. S. Park and Y. B. Shim, *Biosens. Bioelectron.*, 2019, **130**, 48–54, DOI: 10.1016/j.bios.2019.01.028.
9 S. D. Wijayanti, L. Tsvik and D. Haltrich, *Foods*, 2023, **12**(18), 3355, DOI: 10.3390/foods12183355.
10 H. Zhu, F. Shi, M. Peng, Y. Zhang, S. Long, R. Liu, J. Li and Z. Yang, *Chemosensors*, 2025, **13**(1), 19, DOI: 10.3390/chemosensors13010019.
11 J. M. Harris, C. Reyes and G. P. Lopez, *J. Diabetes Sci. Technol.*, 2013, **7**, 1030–1038, DOI: 10.1177/193229681300700428.
12 L. Bourouba, E. Zouaoui, M. Benounis, H. S. Magar and A. Boumaza, *RSC Adv.*, 2025, **15**, 41546–41567, DOI: 10.1039/d5ra07666h.
13 D. Yang, Y. Chen, S. Che and K. Wang, *Coatings*, 2025, **15**(8), 892, DOI: 10.3390/coatings15080892.
14 M. Wang, J. Zheng, G. Zhang, S. Lu and J. Zhou, *Biosensors*, 2025, **15**(5), 309, DOI: 10.3390/bios15050309.
15 M. Eswaran, S. Rahimi, S. Pandit, B. Chokkiah and I. Mijakovic, *Fuel*, 2023, **345**, 128182, DOI: 10.1016/j.fuel.2023.128182.
16 G. Baytemir, Ö. Akay, G. Konuk Ege and N. Taşaltın, *J. Electrochem. Soc.*, 2024, **171**, 127514, DOI: 10.1149/1945-7111/ada067.
17 N. German, A. Popov, A. Ramanavicius and A. Ramanaviciene, *Biosensors*, 2025, **15**(3), 196, DOI: 10.3390/bios15030196.
18 H. Kawakami, Y. Ito, Y. A. Chien, C. Y. Chen, W. T. Chiu, P. Chakraborty, T. Nakamoto, M. Sone and T. F. M. Chang, *Micro Nano Eng.*, 2022, **14**, DOI: 10.1016/j.mne.2022.100109.
19 L. Y. Pan, C. H. Liu, Y. T. Lai, C. Y. Lee, S. Gupta and N. H. Tai, *Microchem. J.*, 2025, **213**, DOI: 10.1016/j.microc.2025.113932.
20 K. Agrahari, Y. W. Wang, C. E. Tsay and Y. H. Cheng, *ACS Appl. Electron. Mater.*, 2025, **7**, 2424–2432, DOI: 10.1021/acsaelm.4c02225.
21 M. I. Pilo, S. Baluta, A. C. Loria, G. Sanna and N. Spano, *Nanomaterials*, 2022, **12**(16), 2840, DOI: 10.3390/nano12162840.
22 S. Baruah, D. Mohanta and C. A. Betty, *Microchem. J.*, 2024, **206**, 111411, DOI: 10.1016/j.microc.2024.111411.
23 Q. Ma, Y. Zhang, L. Wang, Y. Yang and W. Wang, *Microchem. J.*, 2024, **206**, 111574, DOI: 10.1016/j.microc.2024.111574.
24 S. Goswami, S. Nandy, E. Fortunato and R. Martins, *J. Solid State Chem.*, 2023, **317**, 123679, DOI: 10.1016/j.jssc.2022.123679.
25 M. Beygisangchin, S. A. Rashid, S. Shafie, A. R. Sadrolhosseini and H. N. Lim, *Polymers*, 2021, **13**(12), 2003, DOI: 10.3390/polym13122003.
26 A. N. Andriianova, Y. N. Biglova and A. G. Mustafin, *RSC Adv.*, 2020, **10**, 7468–7491, DOI: 10.1039/c9ra08644g.

27 H. N. Heme, M. S. N. Alif, S. M. S. M. Rahat and S. B. Shuchi, *J. Energy Storage*, 2021, **42**, 103018, DOI: 10.1016/j.est.2021.103018.
28 L. Brožová, P. Holler, J. Kovářová, J. Stejskal and M. Trchová, *Polym. Degrad. Stab.*, 2008, **93**, 592–600, DOI: 10.1016/j.polymdegradstab.2008.01.012.
29 M. H. Mostafa, E. S. Ali and M. S. A. Darwish, *Mater. Chem. Phys.*, 2022, **291**, 126699, DOI: 10.1016/j.matchemphys.2022.126699.
30 A. Verma and T. Kumar, *RSC Adv.*, 2024, **14**, 25093–25107, DOI: 10.1039/d4ra04009k.
31 C. Zhang, Q. Chen, X. Ai, X. Li, Q. Xie, Y. Cheng, H. Kong, W. Xu, L. Wang, M. S. Wang, H. Yang and D. L. Peng, *J. Mater. Chem. A*, 2020, **8**, 16323–16331, DOI: 10.1039/d0ta04389c.
32 Z. Benzait, P. Chen and L. Trabzon, *Nanoscale Adv.*, 2021, **3**, 223–230, DOI: 10.1039/d0na00706d.
33 D. D. L. Chung, *J. Mater. Sci.*, 2015, **51**, 554–568, DOI: 10.1007/s10853-015-9284-6.
34 B. Bari, J. Lee, T. Jang, P. Won, S. H. Ko, K. Alamgir, M. Arshad and L. J. Guo, *J. Mater. Chem. A*, 2016, **4**, 11365–11371, DOI: 10.1039/c6ta03308c.
35 G. Eka Putri, F. Rahayu Gusti, A. Novita Sary and R. Zainul, *J. Phys. Conf. Ser.*, 2019, **1317**, DOI: 10.1088/1742-6596/1317/1/012027.
36 S. Kidtang, S. Pimanpang, E. Swatsitang and W. Jarernboon, *ACS Appl. Nano Mater.*, 2025, **8**, 5829–5840, DOI: 10.1021/acsanm.5c00829.
37 M. Xiang, C. Li and L. Ye, *J. Ind. Eng. Chem.*, 2017, **50**, 123–132, DOI: 10.1016/j.jiec.2017.02.005.
38 R. A. G. Rañola, J. M. Kalaw and F. B. Sevilla, *IEEE Sens. J.*, 2016, **16**, 1880–1886, DOI: 10.1109/JSEN.2015.2512612.
39 J. Lai, Y. Yi, P. Zhu, J. Shen, K. Wu, L. Zhang and J. Liu, *J. Electroanal. Chem.*, 2016, **782**, 138–153, DOI: 10.1016/j.jelechem.2016.10.033.
40 V. Osuna, A. Vega-Rios, E. A. Zaragoza-Contreras, I. A. Estrada-Moreno and R. B. Dominguez, *Biosensors*, 2022, **12**(3), 137, DOI: 10.3390/bios12030137.
41 N. Sobahi, M. M. Alam, M. Imran, M. E. Khan, A. Mohammad, T. Yoon, I. M. Mehedi, M. A. Hussain, M. J. Abdulaal and A. A. Jiman, *Molecules*, 2024, **29**(11), 2439, DOI: 10.3390/molecules29112439.
42 B. Gajić, M. Radoičić, M. Yasir, W. Saeed, S. Bolka, B. Nardin, J. Potočnik, G. Ćirić-Marjanović, Z. Šaponjić and S. Jovanović, *Molecules*, 2025, **30**(24), 4693, DOI: 10.3390/molecules30244693.
43 J. Huang, S. Wang, J. Ding, S. Li and J. Xu, *Surfaces and Interfaces*, 2025, **72**, 107065, DOI: 10.1016/j.surfin.2025.107065.
44 Y. Shu, T. Su, Q. Lu, Z. Shang, Q. Xu and X. Hu, *Anal. Chem.*, 2021, **93**, 16222–16230, DOI: 10.1021/acs.analchem.1c04106.
45 Z. Huang, L. Li, Y. Wang, C. Zhang and T. Liu, *Compos. Commun.*, 2018, **8**, 83–91, DOI: 10.1016/j.coco.2017.11.005.
46 A. Boublia, Z. Guezzout, N. Haddaoui, M. Badawi, I. Lakikza, I. Belkhettab, O. Moumeni, S. I. Aouni, M. Alam and Y. Benguerba, *Mater. Adv.*, 2024, **5**, 7349–7376, DOI: 10.1039/d4ma00231h.
47 L. Y. Xu, G. Y. Yang, H. Y. Jing, J. Wei and Y. D. Han, *Nanotechnology*, 2014, **25**(5), DOI: 10.1088/0957-4484/25/5/055201.
48 H. Zafar, A. Channa, V. Jeoti and G. M. Stojanović, *Sensors*, 2022, **22**(2), 638, DOI: 10.3390/s22020638.
49 A. Korent, K. Žagar Soderžnik, S. Šturm and K. Žužek Rožman, *J. Electrochem. Soc.*, 2020, **167**, 106504, DOI: 10.1149/1945-7111/ab9929.
50 Riyanto and M. S. Hakim, *IOP Conf. Ser. Mater. Sci. Eng.*, 2018, **299**, DOI: 10.1088/1757-899X/299/1/012001.
51 Q. Feng, S. O. Ganiyu, E. A. Elimian, L. Xu, Z. Chang and M. Gamal El-Din, *Chem. Eng. J.*, 2025, **512**, 162329, DOI: 10.1016/j.cej.2025.162329.
52 A. Popov, R. Aukstakojyte, J. Gaidukevic, V. Lisyte, A. Kausaite-Minkstimiene, J. Barkauskas and A. Ramanaviciene, *Sensors*, 2021, **21**, 1–15, DOI: 10.3390/s21030948.
53 K. Yang, K. Huang, Z. He, X. Chen, X. Fu and W. Dai, *Appl. Catal., B*, 2014, **158–159**, 250–257, DOI: 10.1016/j.apcatb.2014.04.028.
54 M. E. Ali Mohsin, N. K. Shrivastava, A. Arsad, N. Basar and A. Hassan, *Front. Mater.*, 2020, **7**, DOI: 10.3389/fmats.2020.00020.
55 J. Tarver, J. E. Yoo, T. J. Dennes, J. Schwartz and Y. L. Loo, *Chem. Mater.*, 2009, **21**, 280–286, DOI: 10.1021/cm802314h.
56 Y. Yang, S. Chen, W. Li, P. Li, J. Ma, B. Li, X. Zhao, Z. Ju, H. Chang, L. Xiao, H. Xu and Y. Liu, *ACS Nano*, 2020, **14**, 8754–8765, DOI: 10.1021/acsnano.0c03337.
57 K. W. Jun, J. N. Kim, J. Y. Jung and I. K. Oh, *Micromachines*, 2017, **8**(2), 43, DOI: 10.3390/mi8020043.
58 X. Shen, X. Lin, N. Yousefi, J. Jia and J. K. Kim, *Carbon*, 2014, **66**, 84–92, DOI: 10.1016/j.carbon.2013.08.046.
59 Z. Wang, D. Tonderys, S. E. Leggett, E. K. Williams, M. T. Kiani, R. Spitz Steinberg, Y. Qiu, I. Y. Wong and R. H. Hurt, *Carbon*, 2016, **97**, 14–24, DOI: 10.1016/j.carbon.2015.03.040.
60 K. E. Ramohlola, K. D. Modibane, M. M. Ndipingwi and E. I. Iwuoha, *Eur. Polym. J.*, 2024, **213**, 113125, DOI: 10.1016/j.eurpolymj.2024.113125.
61 Y. Zhang, J. Liu, Y. Zhang, J. Liu and Y. Duan, *RSC Adv.*, 2017, **7**, 54031–54038, DOI: 10.1039/c7ra08794b.
62 B. Butoi, A. Groza, P. Dinca, A. Balan and V. Barna, *Polymers*, 2017, **9**(12), 732, DOI: 10.3390/polym9120732.
63 F. N. Ajjan, M. J. Jafari, T. Rębiś, T. Ederth and O. Inganäs, *J. Mater. Chem. A*, 2015, **3**, 12927–12937, DOI: 10.1039/c5ta00788g.
64 S. Fahad, H. Yu, L. Wang, A. Nazir, R. S. Ullah, K. ur R. Naveed, T. Elshaarani, B. U. Amin, A. Khan and S. Mehmood, *J. Mater. Sci. Mater. Electron.*, 2019, **30**, 12876–12887, DOI: 10.1007/s10854-019-01649-7.
65 S. Sravya, D. RamaDevi, N. Belachew, K. E. Rao and K. Basavaiah, *RSC Adv.*, 2021, **11**, 12030–12035, DOI: 10.1039/d1ra00171j.
66 M. Mitra, S. T. Ahamed, A. Ghosh, A. Mondal, K. Kargupta, S. Ganguly and D. Banerjee, *ACS Omega*, 2019, **4**, 1623–1635, DOI: 10.1021/acsomega.8b02941.

67 L. Zhao, Y. Tan and F. Ran, *J. Mater. Sci. Mater. Electron.*, 2022, **33**, 2138–2151, DOI: 10.1007/s10854-021-07421-0.
68 B. Wang, M. Zhang, W. Li, L. Wang, J. Zheng, W. Gan and J. Xu, *Dalt. Trans.*, 2015, **44**, 7803–7810, DOI: 10.1039/c5dt00003c.
69 W. Li, J. Song, C. Wang, J. Hao, Y. Yang and Z. Yu, *J. Mater. Sci. Mater. Electron.*, 2019, **30**, 5366–5374, DOI: 10.1007/s10854-019-00829-94.
70 S. H. Kim, W. I. Choi, K. H. Kim, D. J. Yang, S. Heo and D. J. Yun, *Sci. Rep.*, 2016, **6**, 33074, DOI: 10.1038/srep33074.